"HOT" NON-FLARING PLASMA IN ACTIVE REGIONS II. IMPACTS OF TWO-FLUID EFFECTS ON EMISSION FROM IMPULSIVELY HEATED LOOPS

W. T. Barnes and S. J. Bradshaw
Department of Physics & Astronomy, Rice University, Houston, TX 77251-1892

P. J. Cargill
Space and Atmospheric Physics, The Blackett Laboratory, Imperial College, London SW7 2BW and
School of Mathematics and Statistics, University of St. Andrews, St. Andrews, Scotland KY16 9SS
Draft version October 5, 2015

ABSTRACT

Faint, high-temperature emission in active region cores has long been predicted as a signature of nanoflare heating. However, the detection of such emission has proved difficult due to a combination of the efficiency of thermal conduction, non-equilibrium ionization, and inadequate instrument sensitivity. This second paper in our series on hot non-flaring plasma in active regions aims to show how the assumption of electron-ion equilibrium in hydrodynamic models leads to incorrect conclusions regarding the hot emission. We have used an efficient two-fluid hydrodynamic model to carry out a parameter exploration in preferentially heated species, nanoflare heating frequency, and event amplitude power-law index. By computing the emission measure distributions and calculating their "hotward" slopes, we have concluded that the assumption of electron-ion equilibrium leads to an understimate of the amount of hot plasma at intermediate and high heating frequencies. Additionally, we find that, while emission due to electron and ion heating differs greatly hotward of the peak, the respective coolward emission measure slopes are similar such that a distinction between the heating of one species over another based on this criteria alone is inadequate.

1. INTRODUCTION

The nanoflare heating model, first proposed by Parker (1988), has become one of the most favored and contentious coronal heating models (Cargill 1994; Cargill & Klimchuk 2004; Klimchuk 2006). While many theoretical efforts (e.g. Bradshaw et al. 2012; Reep et al. 2013) have shown the feasability of nanoflares, the idea has long suffered from a lack observational evidence. The term *nanoflare* has now become synonomous with impulsive heating in the energy range $10^{24} - 10^{27}$ ergs, with no specific assumption as to what underlying physical mechanism is responsible. However, while we ascribe no particular source (e.g. wave versus reconnection) to this bursty energy release, its origin is almost certainly magnetic.

Cargill (1994); Cargill & Klimchuk (2004) have predicted that emission measure distributions resulting from nanoflare models should be wide and have a faint, high-temperature ($> 4 \times 10^6$ K) component and thus a steep hotward slope, the so-called "smoking gun" of nanoflare heating. Unfortunately, observing this high-temperature emission is difficult and in some cases impossible. The reason for this difficulty is twofold. First, thermal conduction is a very efficient cooling mechanism at high temperatures and large spatial temperature gradients. When a loop is heated impulsively, its temperature rises quickly while the increase in density lags behind. By the time the density has increased sufficiently to allow for an appreciable amount of emission (recalling EM $\propto n^2$), thermal conduction has cooled the loop far below its initial hot temperature, making a direct detection of > 10 MK

will.t.barnes@rice.edu

plasma very difficult.

The second reason for this difficulty is non-equilibrium ionization. It is usually assumed that the observed line intensities, because of their known formation temperatures, are a direct indicator of the plasma temperature. However, if the heating timescale is shorter than the ionization timescale, the time it takes for the ion population to settle into the correct charge state, an equilibrium assumption can lead to a misdiagnosis of the plasma temperature. This makes signatures of hot, nanoflare-heated plasma especially difficult to detect if the high temperatures persist for less than the ionization timescale (Bradshaw & Cargill 2006; Bradshaw & Klimchuk 2011; Reale & Orlando 2008).

Despite these difficulties, various attempts have been made to observe this faint high-temperature emission. Using the broadband X-Ray Telescope (XRT) aboard the *Hinode* spacecraft, Schmelz et al. (2009) and Reale et al. (2009) show a faint hot component in the reconstructed DEM curves. However, since the channels on such broadband instruments can often be polluted by low-temperature emission, the reliability of such measurements depends on the filtering technique used. Additionally, Winebarger et al. (2012) showed that combinations of measurements from EIS (Culhane et al. 2007) and XRT (Golub et al. 2007) on board *Hinode* (Kosugi et al. 2007) leave a "blind spot" in the EM $- T$ space coinincident with where evidence for nanoflare heating is likely to be found.

Unambiguous observational evidence of nanoflare heating must come from pure spectroscopic measurements (see Brosius et al. 2014). Additionally, new instruments with higher spatial and temporal resolution, such as *IRIS* (De Pontieu et al. 2014) and the *Hi-C* sounding rocket

(Cirtain et al. 2013) have provided encouraging results for impulsive heating (Testa et al. 2013, 2014). Future missions like the Marshall Grazing Incidence X-ray Spectrometer (MaGIXS) (Kobayashi et al. 2011; Winebarger 2014), with a wavelength range of 6-24 Å and a temperature range of $6.2 < \log T < 7.2$, aim to probe this previously poorly-resolved portion of the coronal spectrum in hopes of better quantifying the presence of faint, high-temperature plasma.

One strategy for constraining the nanoflare model is analysis of modeled and observed emission measure distributions for signatures of impulsive heating in active region cores. As with cool emission, hot emission is also often characterized by EM $\propto T^a$. Typically, this linear fit on $\log T, \log EM$ is done "hotward" of the peak, usually in the range $6.6 \lesssim \log T \lesssim 7.2$. However, measured values of these hotward slopes are poorly constrained due to both the magnitude of emission and the lack of available spectroscopic data in this temperature range. Warren et al. (2012), using spectral measurements from EIS, provided hotward fits for EM reconstructions for a large number of active regions. All measured slopes fell in the range $6.1 < |a| < 10.3$, with large uncertainties on each hotward fit.

An often overlooked consequence of impulsive heating in the corona is electron-ion non-equilibrium. In a fully-ionized hydrogen plasma like the solar corona, interactions between electrons and ions occur through binary Coulomb collisions. For $n \sim 10^8$ cm^{-3} and $T \sim 10^7$ K, parameters typical of nanoflare heating, the collisional timescale, $\tau_{ei} = 1/\nu_{ei}$, where ν_{ei} is the Coulomb collision frequency (see Equation A6) can be estimated as $\tau_{ei} \sim \approx 8000$ s. Thus, any heating that occurs on a timescale less than 8000 s, such as a nanoflare with a durration of ≤ 100 s, will result in electron-ion non-equilibrium.

The degree to which the ions or electrons are preferentially heated in the solar corona is unknown though it is often assumed that the electrons are the direct recipients of the prescribed heating function. However, it is also possible that the ions are preferentially heated; for instance, through ion-cyclotron wave resonances (Markovskii & Hollweg 2004). Ion cyclotron waves are excited by plasma instabilities in the lower corona. These waves then propagate upwards through the coronal plasma and wave particle interactions can occur for those ions whose gyrofrequencies have a resonance with the ion-cyclotron wave. Additionally, there is also evidence for ion heating via reconnection, both in laboratory plasmas and in particle-in-cell simulations (Ono et al. 1996; Yoo et al. 2014; Drake & Swisdak 2014). Thus, ion heating in the solar corona should not be discounted as a possibility.

In our first paper, Cargill et al. (2016)(Paper I, hereafter), we studied the effect of pulse duration, flux limiting, and non-equilibrium ionization on hot emission from single nanoflares as well as nanoflare trains. In this second paper in our series on hot emission in active region cores, we will use an efficient two-fluid hydrodynamic model to explore the effect of electron and ion heating on nanoflare-heated loops. In particular, we will look at how the hot emission is affected by heating preferentially one species or the other as well as how this hot emission can vary with heating frequency and event amplitude

power-law index.

Section 2 discusses the numerical model we have used to conduct this study and the parameter space we have explored. Section 3 shows the resulting emission measure curves and slopes for the electron and ion heating cases as well as the equivalent single-fluid cases. In Section 4, we discuss the implications of two-fluid effects in the context of hot and cool emission measure slopes and the nanoflare heating model. Finally, Section 5 provides some concluding comments on our findings.

2. METHODOLOGY

2.1. *Numerical Model*

1D hydrodynamic models are excellent tools for computing field-aligned quantities in coronal loops. However, because of the small grid sizes needed to resolve the transition region and consequently small timesteps needed to resolve thermal conduction, the use of such models in large parameter sweeps is made impractical by long runtimes (Bradshaw & Cargill 2013). Thus, in our numerical study, we will use a modified form of the popular 0D enthalpy-based thermal evolution of loops (EBTEL) model (Klimchuk et al. 2008; Cargill et al. 2012a,b, 2015) which computes time-dependent spatially-averaged loop quantities and has been successfully benchmarked against the 1D hydrodyhnamic HYDRAD code (Bradshaw & Cargill 2013).

We have modified the usual EBTEL equations (see Cargill et al. 2012a) to treat the evolution of the electron and ion populations separately while maintaining the assumption of quasi-neutrality, $n_e = n_i = n$. This amounts to computing spatial averages of the two-fluid hydrodynamic equations over both the transition region and corona. We will reserve a full discussion of this modified EBTEL model for a future paper. The relevant equations can be found in Appendix A.

2.2. *Parameter Space*

We define our heating function in terms of a series of discrete heating events plus a static background heating rate to ensure that the loop does not drop to unphysically low temperatures and densities between events. All events are modeled as triangular pulses of fixed duration $\tau_H = 100$ s. Thus, for loop length L and cross-sectional area A, the total energy per event is $Q_i = LAH_i\tau_H/2$, where H_i is the heating rate amplitude for the ith event. Each run will consist of N heating events, with peak amplitude H_i and a steady background value of $H_b = 3.4 \times 10^{-6}$ erg cm^{-3} s^{-1}.

Observations have suggested that loops in active region cores are maintained at an equilibrium temperature of $T_{peak} \approx 4$ MK (Warren et al. 2011, 2012). The corresponding heating rate can be estimated using coronal hydrostatics. Neglecting the radiative loss term and letting $dF_C/ds \approx \kappa_0 T_{peak}^{7/2}/L^2$, $E_{H,eq}$ can be estimated as

$$E_{H,eq} \approx \frac{\kappa_0 T_{peak}^{7/2}}{L^2},\tag{1}$$

where $\kappa_0 \approx 10^{-6}$. $E_{H,eq}$ can be interpreted as a time-averaged volumetric heating rate. Thus, to maintain an emission measure peaked about T_{peak}, for triangular pulses, the individual heating rates are constrained
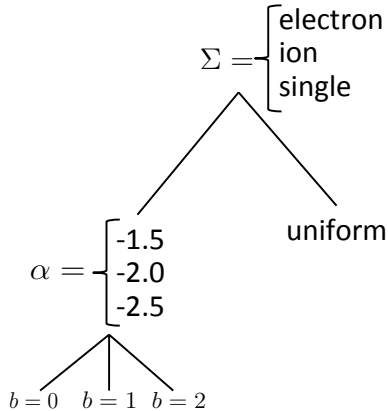
FIG. 1.— Parameter space covered for each loop half-length L. Σ indicates the species that is heated, where "single" indicates a single-fluid model. α is the power-law index and b indicates the scaling in the relationship $Q \propto T_N^b$, where $b = 0$ corresponds to the case where T_N and the event energy are independent.

by

$$E_{H,eq} = \frac{1}{T} \sum_{i=1}^{N} \int_{t_i}^{t_i+\tau_H} \mathrm{d}t\ h_i(t) = \frac{\tau_H}{2T} \sum_{i=1}^{N} H_i. \quad (2)$$

Note that if $H_i = H_0$ for all i, the uniform heating amplitude H_0 is just $H_0 = 2TE_{H,eq}/N\tau_H$. Thus, for $L = 40$ Mm, $A = 10^{14}$ cm^2, the total amount of energy injected into the loop by one heating event for a loop heated by $N = 20$ nanoflares in $T = 80000$ s is $Q = LATE_{H,eq}/N \approx 1.3 \times 10^{25}$ erg, consistent with the energy budget of the Parker nanoflare model.

Determining the heating frequency in active region cores will help to place constraints on the source(s) of heat in the corona. We define the heating frequency in terms of the waiting time, T_N, between successive heating events. Following Cargill (2014), the range of waiting times is $250 \leq T_N \leq 5000$ s in increments of 250 s, for a total of 20 different possible heating frequencies. Additionally, T_N can be written as $T_N = (T - N\tau_H)/N$, where $T = 80000$ s is the total simulation time. Note that because T and τ_H are fixed, as T_N increases, N decreases. Correspondingly, Q_i, the energy injected per event, increases according to Equation 2 such that the total energy injected per run is constant, regardless of T_N.

We compute the peak heating rate per event in two different cases: 1) uniform heating rate such that $H_i = H_0$ for all i and 2) H_i chosen from a power-law distribution with index α where $\alpha = -1.5, -2.0, -2.5$. For the second case, it should be noted that, when T_N is large, $N \sim 20$ events, meaning a single run does not accurately represent the distribution of index α. Thus, a sufficiently large number of runs, N_{MC}, are computed for each T_N to ensure that the total number of events is $N_{tot} = N \times N_{MC} \sim 10^4$ such that the distribution is well-represented. Figure 1 shows the parameter space we will explore. For each point in (Σ, α, b) space, the response to $\sim N_{tot}$ events for each waiting time T_N will be computed.

According to the nanoflare heating model of (Parker 1988), turbulent loop footpoint motions twist and stress the field, leading to a buildup and subsequent release of
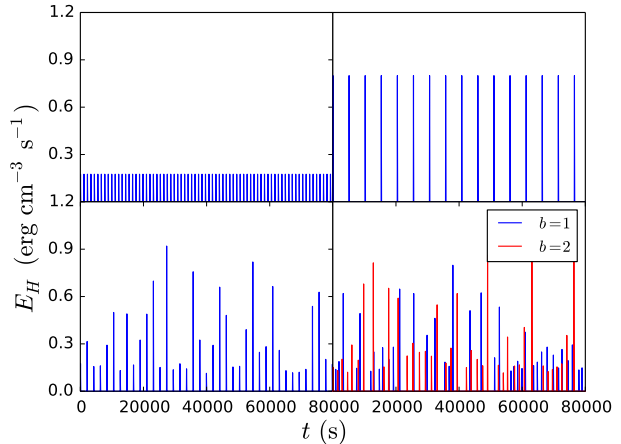

FIG. 2.— All heating functions are for $L = 40$ Mm. Starting counter-clockwise from the bottom left: uniform heating amplitudes for $T_N = 1000$ s; uniform heating amplitudes for $T_N = 5000$ s; power-law distributed heating amplitudes for $\alpha = -1.5$, $T_N = 2000$ s; power-law distributed amplitudes for $\alpha = -1.5$ where the wait times depend on the event energies and the mean wait time for both b values is $\langle T_N \rangle = 2000$ s.

energy. Following Cargill (2014), we let $Q_i \propto T_{N,i}^b$, where $Q_i, T_{N,i}$ are the total energy and waiting time following the ith event, respectively, and $b = 1, 2$. The reasoning for such an expression is as follows. Bursty, nanoflare heating is thought to arise from the stressing and subsequent relaxation of the coronal field. If a sufficient amount of time has elapsed since the last energy release event, the field will have had enough time to "wind up" such that the subsequent energy release is large. Conversely, if only a small amount of time has elapsed since the last event, the field will have not had time to become as stressed, resulting in a lower energy event. Thus, this scaling provides a way to incorporate a more realistic heating function into a hydrodynamic model which cannot self-consistently determine the heat input based on the evolving magnetic field. Figure 2 shows the various heating functions used for several example T_N values.

2.3. Emission Measure Distributions

In our 0D model, the emission measure is calculated using the familiar expression $\mathrm{EM}(T) = n^2(2L)$, where L is the loop half-length. We consider a temperature range of $4.0 \leq \log T \leq 8.5$ with bin sizes of $\Delta \log T = 0.01$. At each iteration i, the coronal temperature range $[T_0, T_a]$ is calculated from $\bar{T}_e$ (see Appendix A). For each bin that falls within $[T_0, T_a]$, $\bar{n}_i^2 L$ is added to that bin, where $\bar{n}_i$ is the spatially-averaged number density at the ith iteration. After all iterations have completed, the emission measure in each bin is averaged over the entire simulation period. We do not attempt to apply an advanced forward modeling treatment here and instead reserve such an approach for a future paper. Thus, effects due to insufficient instrument sensitivity or non-equilibrium ionization are not included.

3. RESULTS

For each species, power-law and wait-time index, (α, b), and waiting time T_N, N_{MC} emission measure curves are calculated. Because drawing event amplitudes from a

power-law distribution introduces random fluctuations into our model, we must be sure to account for the full range of effects due to the distribution. This is especially true in the low-frequency regime, when $T_N \geq \tau_{cool}$, and there are fewer events per run. In this case, one or two especially strong heating events can lead to an extremely enhanced hotward emission measure; conversely, a run with only small events will lead to a diminished hotward slope. Thus, the mean $EM(T)$ curve of each set of N_{MC} runs can be said to reasonably represent the expected hot emission for a given T_N.

To characterize the emission measure, we compute the slopes on both the cool and hot sides of the peak. To be consistent with past observational and computational studies of cool emission (see Bradshaw et al. 2012, and references therein), we fit the cool slope on the interval $6.0 \leq \log T \leq 6.6$ in . Contrastingly, past studies of hot emission are less abundant; thus, the region where $\log EM(T)$ is known to be linear is far less constrained. In order to best describe the steepness of the emission measure hotward of the peak, we choose to fit $EM(T)$ between the temperature at which the emission measure is 99% of the peak value and 92% of the peak value. We have no physical reason for choosing these particular bounds, but note that on this interval, the mean hotward emission is reasonably well described by a linear relationship. Fitting too close to the wide peak leads to misleadingly shallow slopes while fitting too close to the steep drop near $\log T \sim 7.5$ results in steep slopes not particularly representative of the hotward emission. We perform the fit using the Levenberg-Marquardt algorithm for least-squares curve fitting as implemented in the SciPy scientific Python package (van der Walt et al. 2011).

3.1. *Electron and Ion Heating*

Figure 3 and Figure 4 show the results of our emission measure study for the cases of electron heating and ion heating with $\alpha = -2.5, b = 1$ for a loop half-length of 40 Mm, consistent with Paper I. The panels on the left show the mean $EM(T)$ for all T_N, where the average is taken over all N_{MC} runs. There is an artifical spacing of $\Delta \log EM = 0.2$ between each curve so that they can be easily distinguished from each other. The blue (red) lines indicate the cool (hot) linear fits, where the slopes of the lines are the averages taken over all N_{MC} runs. We note that $EM(T)$, for all T_N, peaks at approximately 4 MK$\approx 10^{6.6}$ K, consistent with the constraints laid out in Subsection 2.2. The top right panels show these average slope values as a function of T_N. The error bars indicate one standard deviation as calculated from the distribution of all N_{MC} runs. In the case of the hot slopes, the absolute value of the slope is shown since all of the hotward slopes are less than zero.

Lastly, the bottom right panels show the first derivative as a function of temperature, $d \log EM/d \log T$, computed using central differences. The color scheme and line styles correspond to the emission mesure curves in the left panel. As in Paper I, we compute the derivative in an effort to better assess at what temperatures the emission measure is not well described by a linear fit.

We first briefly consider the calculated cool emission measure slopes. Looking at the top right panels of 3 and 4, we note that in the cases of electron and ion heat-

ing, the cool emission measure slopes are consistent with both observational and modelling studies of cool emission in active region cores, having values that fall within the range $2 \leq a \leq 5$ (Bradshaw et al. 2012, and references therein). Furthermore, the cool slopes computed using our new modified EBTEL model, with a heating function of the form $Q \propto T_N$, are consistent with those values reported in Cargill (2014) and show a moderate dependence on the waiting time T_N.

Additionally, looking at the bottom right panels of Figure 3 and Figure 4, we see that, within the range $6.0 \leq \log T \leq 6.6$, a linear approximation of EM on a log-log scale is reasonable, where $2 \lesssim d \log EM/d \log T \lesssim 3$. Comparing the cases of electron and ion heating for both the cool slopes and $d \log EM/d \log T$ on $6.0 \leq \log T \leq 6.6$, there are no substantial differences for all values of T_N considered.

This is not the case for the hot emission measure. Looking first at the case of electron heating in Figure 3, we note that there is a pronounced "hot shoulder" in the emission measure (left panel) just above 10^7 K for $T_N \gtrsim 2000$. This feature is even more evident when looking at the derivative of $EM(T)$ in the bottom right panel of Figure 3. The peak between 10^7 and $10^{7.5}$ K shows how $EM(T)$ flattens out around 10^7 K, indicating an enhanced hot emission measure. Considering the large range of values of $d \log EM/\log T$ on the interval over which the linear fit was performed, we acknowledge that a simple linear fit is not a good description of the hot emission measure in the case of electron heating.

Contrastingly, we have not calculated the hot emission measure slopes for the case of ion heating. Looking at the left panel of Figure 4, for $T_N \gtrsim 1000$ s, the $EM(T)$ peak is wide with a steep drop near 10^7 K. There is no substantial emission measure component above 10^7 K and, consequently, no hot shoulder as in the electron heating case. Applying the fitting procedure outlined above to the hot emission in the case of ion heating yields meaningful results for only a few low values of T_N. Thus, like the case electron heating, the resulting hot emission measure from ion heating is not well described by a linear relationship in $\log EM, \log T$. The lower right panel of Figure 4 further highlights this by showing that around 10^7 K, $d \log EM/d \log T \to -\infty$.

3.2. *Single-fluid*

Figure 5 shows the same results as Figure 3 and Figure 4, but for the single-fluid case in which electron-ion equilibrium is assumed at all times. To compute these $EM(T)$ curves, we have used the original, single-fluid EBTEL model as described in Klimchuk et al. (2008); Cargill et al. (2012a). The equivalent parameter space that was investigated with the modified two-fluid EBTEL model is explored with the single-fluid EBTEL code as well.

We compute the hot and cool emission measure slopes in the same manner as the electron and ion heating cases. We first note that the cool emission measure slopes are comparable to those in both the electron and ion heating cases. In particular, we find $2 \lesssim a \lesssim 5$ for all values of T_N as expected. Again, we confirm the validity of our linear fit to the cool emission by computing the derivative $d \log EM/d \log T$ in the lower right panel of Figure 5. For $T_N \gtrsim 2000$ s, the slope is bounded between 2 and 3 on
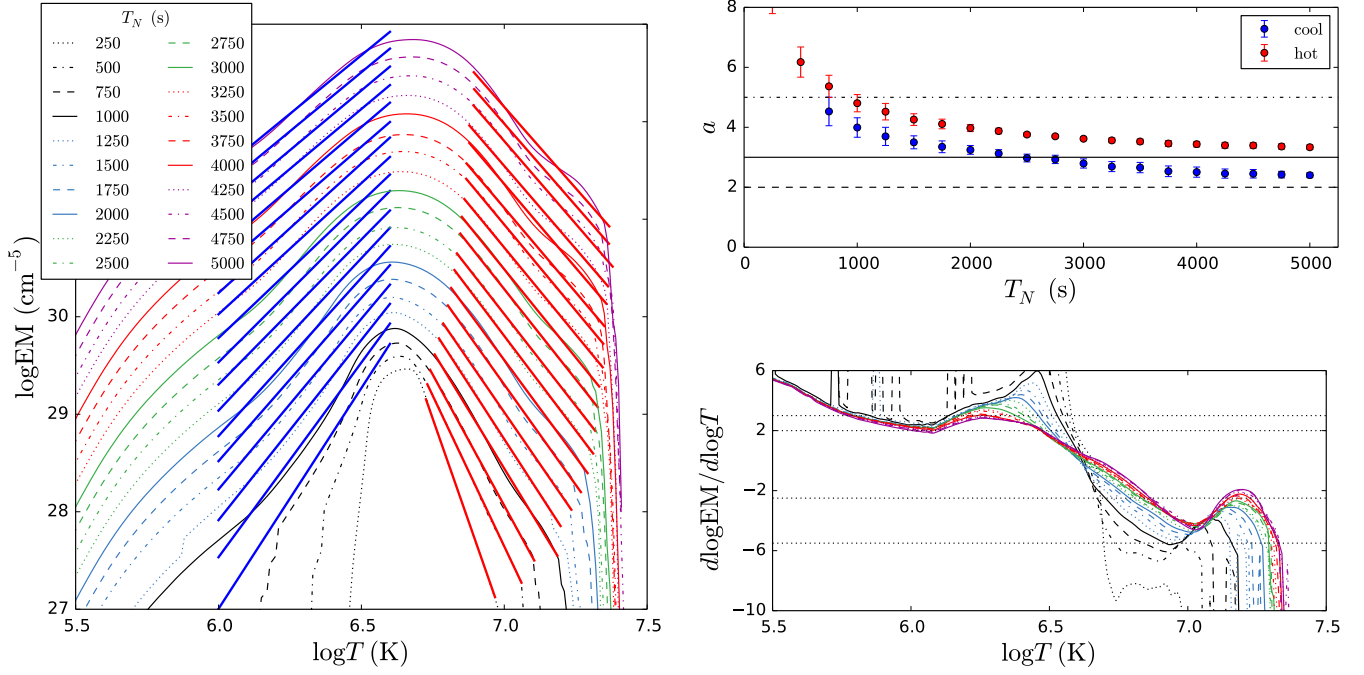
Fig. 3.— $\alpha = -2.5$, $b = 1$, $L = 40$ Mm, electron heating. **Left:** $\log \mathrm{EM}(T)$ as a function of $\log T$ for all values of T_N. There is an artificial spacing of $\Delta \log \mathrm{EM} = 0.2$ between each curve for aesthetic purposes. The bold blue (red) lines on either side of the peak show the linear fit to the cool (hot) emission. **Top right:** Average slopes from linear fit to all N_{MC} curves as a function of T_N. The error bars indicate one standard deviation from the distribution of N_{MC} fits. In the case of hot slopes, the absolute value is shown. **Bottom right:** Derivative of $\log \mathrm{EM}$ with respect to $\log T$. The legend is the same as the left panel.
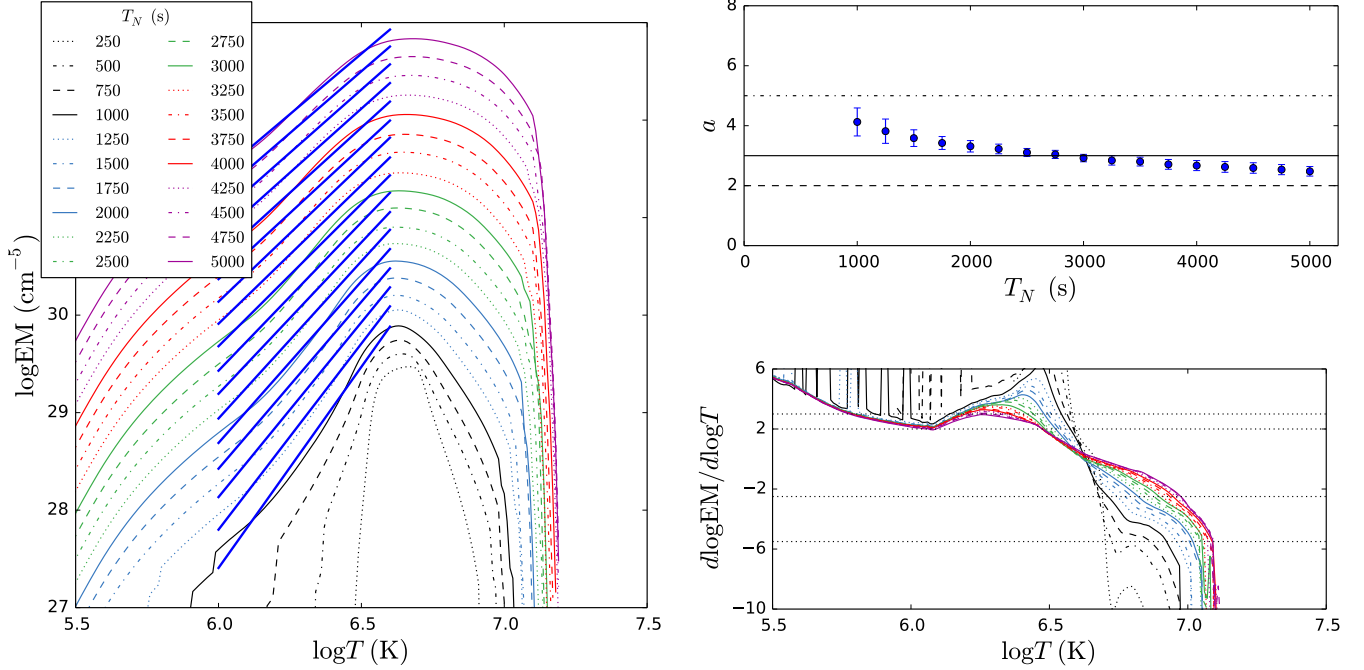

Fig. 4.— Same as Figure 3, but for the case in which all of the heating is given to the ions.

the interval $6.0 \leq \log T \leq 6.6$.

The hot emission measure in the single-fluid case differs significantly from the two-fluid case. In contrast to the electron heating case in Figure 3, the EM curves in the left panel of Fig. Figure 5 show no hot shoulder. This is further confirmed by the lower right panel; the derivative, in contrast to the electron heating case, shows no peak near 10^7 K. For low T_N, $d \log \mathrm{EM} / d \log T$ is monotonically decreasing for $\log T \gtrsim 6.6$. For $T_N \geq 3000$ s, $d \log \mathrm{EM} / d \log T$ is relatively flat for $\log T \geq 7.0$, indicating that a linear fit is a good description for the hot emission in this region. This is confirmed by noting the agreement between the fit lines and the $\mathrm{EM}(T)$ curves in the left panel.

Comparing the top right panels of Figure 5 and Figure 3 further highlights the enhanced hot emission in the electron case. For high T_N, the hot emission slope in the electron case converges to a value just above 3; the single-fluid case, the hot slope converges to approximately 4.5. Thus, while a linear fit is not a good descriptor of the hot emission in the case of electron heating, the slope still captures the enhanced hot shoulder relative to the weaker hot emission of the single-fluid case. Additionally, comparing the single-fluid case to the ion heating case in Figure 4, it is obvious that the single-fluid case shows a great deal more hot emission as the $\mathrm{EM}(T)$ curves in the left panel of Figure 5 extend well above 10^7 K while those in the left panel of Figure 4 show a steep cutoff at temperatures just above the peak.

3.3. *Full Parameter Space Comparison*

To compare the effects of varying α, b, and T_N for each species (i.e. electron, ion, single-fluid), we construct histograms of hot and cool emission measure slopes for each parameter space point. Recall that in the case where the heating event amplitudes are non-uniform, we have N_{MC} emission measure slopes so as to properly account for the statistical spread in hot emission measure slopes due to power-law distributions.

As seen in Figure 6, these histograms, denoted by type of slope (i.e. hot or cool) and species, are constructed in one of two ways: each distinct histogram (denoted by linestyle and/or color) is either representative of a distinct heating function (e.g. top row of Figure 6) or a distinct value of T_N (e.g. bottom row of Figure 6). In the four panels of Figure 6, we choose to separate the cool emission measure slopes by type of heating function and the hot emission measure slopes by T_N. This means, for example, that the dot-dashed blue $\alpha = -1.5, b = 2$ histogram in the upper left panel of Figure 6 encapsulates cool emission measure slopes for $250 \leq T_N \leq 5000$ s while the solid blue $T_N = 2000$ s histogram in the lower left panel includes emission measure slopes for all 10 types of heating functions (as listed in Figure 1 and the legend in the upper left panel of Figure 6). All histograms are normalized such that for each distribution $P(x)$, $\int_{-\infty}^{\infty} \mathrm{d}x \, P(x) = 1$. Additionally, the bin widths are calculated using the well-known Freedman-Diaconis formula (Freedman & Diaconis 1981).

Concerning the distributions of cool slopes grouped by type of heating function (bottom row of Figure 6), we note that there are no discernible differences between the cases of electron and ion heating. In both cases, all heating functions except for those where $b = 1$ are peaked

sharply between 2 and 2.5. In the case where $b = 1$ (for all α), the distribution is peaked between 2.5 and 3, with the width of the distribution increasing as the power-law index steeps. This larger range of cool emission measure slopes for the case of $b = 1$ is consistent with Cargill (2014).

As stated in Subsection 3.1, we choose not to show the hot emission measure slopes for the ion heating case as they are not a good descriptor of the emission measure distribution hotward of the peak as evidenced by the left and bottom right panels of Figure 4. Instead, we compare the hot emission measure slopes of the electron heating and single-fluid cases, the bottom left and right panels of Figure 6, respectively. In both cases, for $T_N < 3000$ s, we see a strong dependence on T_N while for $T_N \geq 3000$ s, the slopes tend to be sharply peaked around a single value. In the electron heating case, distributions for $T_N < 3000$ s tend to be more narrow than their single-fluid counterparts and centered at lower values (i.e. more shallow hot slopes). Most notably, for $T_N \geq 4000$ s, the electron heating hot emission measure slopes are peaked between 3 and 3.5 while the single-fluid slopes are peaked at ~ 4.5.

4. DISCUSSION

The main points we emphasize from the results presented in Section 3 are,

1. Cool emission measure slopes resulting from electron and ion heating are very similar and are well described by $\mathrm{EM} \propto T^a$. As noted in Cargill (2014), using the relation $Q \propto T_N$ yields $2 \lesssim a \lesssim 5$, consistent with observations.

2. Hot emission from electron heating results in an enhanced hot shoulder while the equivalent ion heating cases show a relatively flat peak and a steep dropoff near 10^7 K. This effect is exacerbated as T_N increases.

3. Hot emission due to both electron and ion heating is poorly described by the scaling $\mathrm{EM} \propto T^a$. In the former, this is due to the flat hot shoulder between 10^7 and $10^{7.5}$ K. In the latter case, the relatively flat peak and steep drop off near 10^7 K do not allow for a power-law description of the hot emission.

4. Single-fluid models predict less hot-emission than two-fluid models in which only the electrons are heated. In particular, for $T_N \geq 4000$ s, our modified two-fluid EBTEL model predicts $3 \leq a \leq 3.5$ while the original single-fluid EBTEL model predicts $a \sim 4.5$.

We first focus on item 1. In the range $6.0 \leq \log T \leq 6.6$, the loop is undergoing both radiative and enthalpy-driven cooling. During this phase, the density is high and the temperature low relative to the heating and conductive cooling phase. Looking at the fourth term on the right-hand side of Equation A1 and Equation A6, the coupling term between the two species is roughly $\propto \bar{n}^2(\bar{T}_e - \bar{T}_i)/\bar{T}_e^{3/2}$; as density increases, so does the coupling strength. While the loop is also draining in this temperature range, the density has already increased such that $\bar{T}_e \approx \bar{T}_i$ and until the next heating event, there is nothing to drive the two species out of equilibrium. Thus, because the two-species are in equilibrium in this
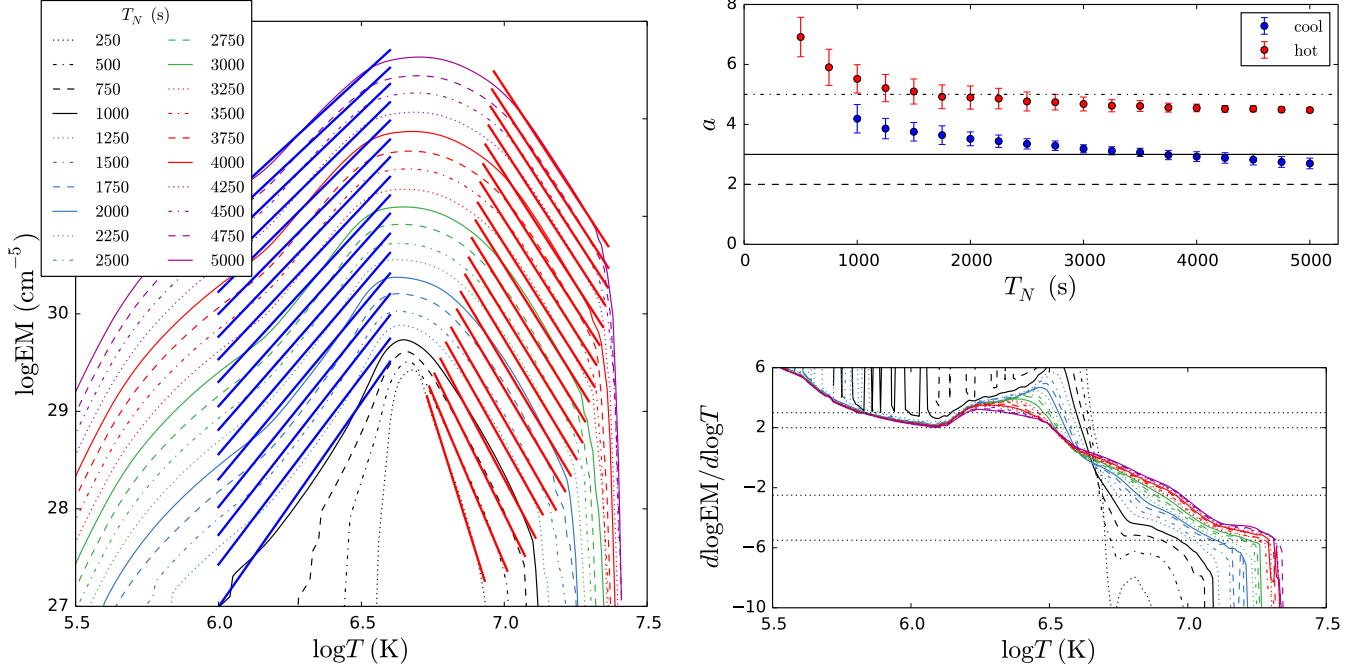
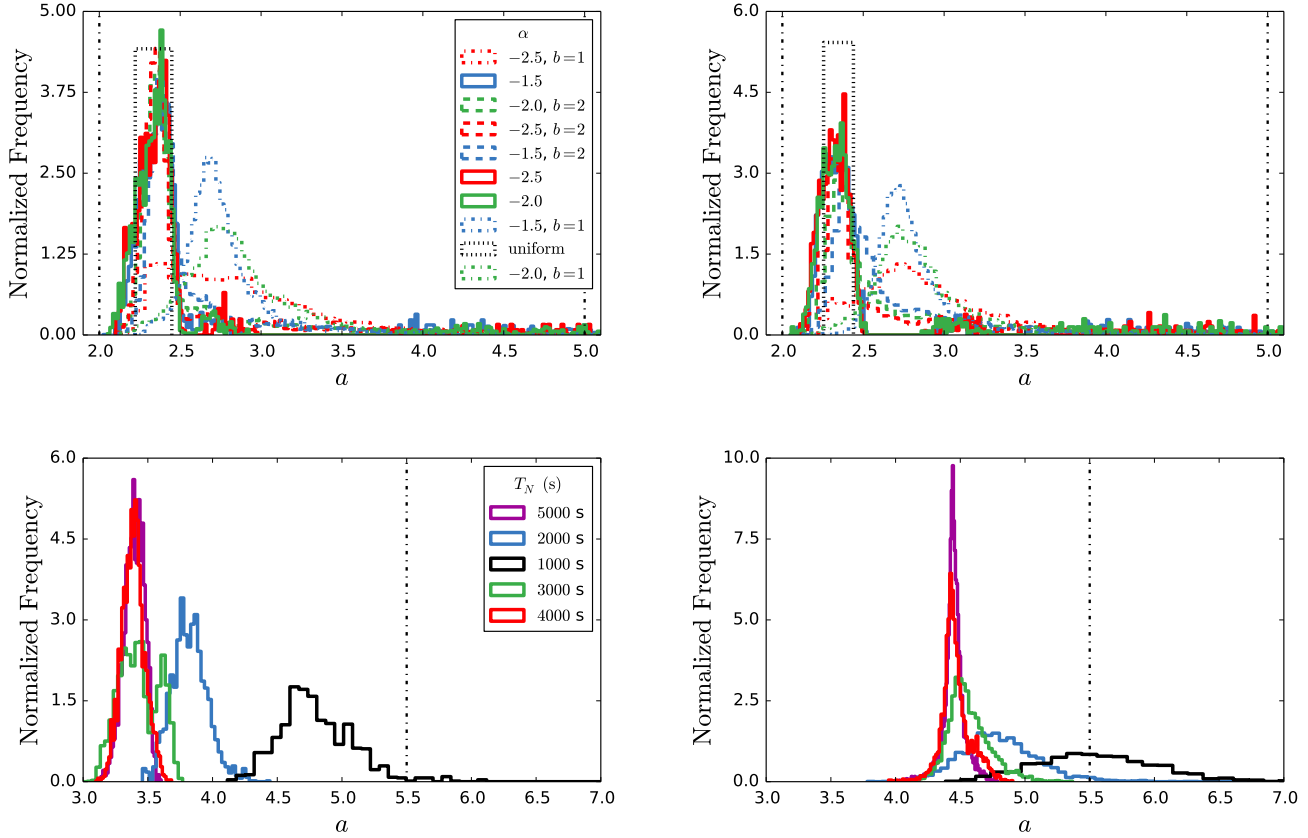FIG. 5.— Same as Figure 3, but for the single-fluid case in which electron-ion equilibrium is assumed.

FIG. 6.— Histograms of emission measure slopes from the entire parameter space as described in Figure 1. Clockwise from top left: cool slopes grouped by heating function for the electron heating case; cool slopes grouped by heating function for the ion heating case; hot slopes grouped by T_N value for the single-fluid case; hot slopes grouped by T_N for the electron heating case. In the cases where the slopes are grouped by T_N, only $T_N = 1000, 2000, 3000, 4000, 5000$ s are shown for aesthetic purposes.

regime, we expect there emission measure distributions to be the same.

In item 2, we see quite the opposite situation. In the heating and conductive cooling phases, the density is relatively low and the electron (or ion) temperature relatively high. Because the heating pulses we have used are relatively short (100 s), the temperature of the heated species reaches high temperatures and cools significantly by thermal conduction before Coulomb collisions can bring the two species back into equilibrium. Since the emission measure depends on the electron temperature, this means that in the event that only the electrons are heated, the emission "sees" the full range of temperatures produced by heating and conductive cooling.

However, in the case of ion heating, in order for the emission measure to see the full range of temperatures resulting from the heating and conductive cooling by the ions, $\bar{T}_e = \bar{T}_i$ would have to hold for this entire phase. Instead, as the ions are impulsively heated, the electrons remain at a relatively low temperature, coupled only weakly to the ions because the loop has not yet begun to fill. As the loop fills, the electrons come into equilibrium with the ions, but because thermal conduction is such an efficient cooling mechanism in the corona, the ions have now cooled far below their temperature to which they were initially heated. The result is a severely truncated hot emission measure distribution as seen in Figure 4. Additionally, this affect is exacerbated at high T_N. At low T_N, the heating is essentially steady, meaning that the loop has no time to drain or cool between heating events. This keeps the density at a constant, near-equilibrium value which inhibits thermal conduction and keeps the electrons and ions in equilibrium. However, for larger values of T_N, the loop is allowed to drain significantly between each pulse. Thus, at the start of each heating event, the density is low, allowing the species to very quickly evolve out of equilibrium.

To address item 3 and item 4, we refer to our discussion in the introduction of Paper I. Using EM $\sim n^2\tau_{cool}$ and assuming constant pressure (such that $n \propto T^{-1}$), in the free-streaming regime, EM $\propto T^{-5/2}$, and in the regime described by classical Spitzer conduction, EM $\propto T^{-11/2}$. Thus, at high temperatures where the free-streaming limit is imposed to prevent runaway cooling by thermal conduction, we expect a much more shallow emission measure slope than at slightly lower temperatures where Spitzer conduction dominates.

Significant emission in the free-streaming regime is produced in the case of electron heating as evidenced by the hot shoulder in the emission measure curves of Figure 3. The derivative in the lower-left panel also clearly shows the slope varying between roughly 5.5 and 2.5 as denoted by the two lower black dotted lines. Fitting a single slope to this entire range, we would expect the resulting slope to be between 2.5 and 5.5 which is indeed the case as evidenced by the bottom-left panel of Figure 6. When characterizing such hot emission in the future, it may be more applicable to fit this emission with a double power-law in order to more properly account for these two distinct cooling regimes.

In the single-fluid case, the free-streaming limit is not reached because the heating is essentially equally par-

titioned between the electrons and ions, resulting in a steeper distribution described by a single power-law. In the case of ion heating, the emission measure never sees this temperature regime because the collisional coupling timescale is significantly longer than the heating timescale.

5. CONCLUSIONS

In this paper, we have used a modified two-fluid version of the popular EBTEL model to study the effect of preferentially heating the electrons or ions on the hot and cool emission measure slopes over a parameter space that includes event amplitude power-law index α, waiting time between successive heating events T_N, and the scaling between the event energy and wait time, b. We have found that while there is little difference in the cool emission between the cases of electron and ion heating, when it comes to the hot emission, the emission measure curves of the electron-heated loops have an enhanced hot shoulder while the ion-heated loops show a truncated emission measure distribution on the hot side. This difference becomes more prominent as T_N increases. Furthermore, by comparing these results with emission measure distributions obtained from the original single-fluid EBTEL model, we have found that heating only the electrons leads to significantly shallower hot emission measure slopes for equivalent values of T_N. Thus, using a single-fluid model to interpret observed hot emission measure could potentially lead to a misdiagnosis of the heating frequency.

We note that in this study, we have constructed the most ideal emission measure curves by using the expression EM $= n^2L$; that is, we have not taken into account the many complications involved when computing emission measure distributions from observed spectral lines. For example, as we noted in Paper I, impulsive heating leads to non-equilibrium ionization and a consequently lower effective temperature, meaning that the emission does not see the hottest temperatures during the conductive cooling phase. Incorporating non-equilibrium ionization will thus steepen the emission measure distribution, leading to larger emission measure slopes.

Additionally, using a more advanced forward modeling technique in the manner of (Bradshaw & Klimchuk 2011) in which the limitations of both the instrument and the atomic data are taken into account will likely further steepen the hot emission distribution. Thus, we stress that, when interpreting observed hot emission in the context of simulation, two-fluid, non-equilibrium ionization, and instrument effects should all be properly taken into account in order to extract meaningful properties of the heating.

APPENDIX

The modified two-fluid EBTEL equations are,

$$\frac{d}{dt}\bar{p}_e = \frac{\gamma - 1}{L}[\psi_{TR} + \psi_C - (\mathcal{R}_{TR} + \mathcal{R}_C)] + k_B \bar{n}\nu_{ei}(\bar{T}_i - \bar{T}_e) + (\gamma - 1)\bar{E}_{H,e}, \tag{A1}$$

$$\frac{d}{dt}\bar{p}_i = -\frac{\gamma - 1}{L}(\psi_{TR} + \psi_C) + k_B \bar{n}\nu_{ei}(\bar{T}_e - \bar{T}_i) + (\gamma - 1)\bar{E}_{H,i}, \tag{A2}$$

$$\frac{d}{dt}\bar{n} = \frac{c_2(\gamma - 1)}{c_3 \gamma L k_B \bar{T}_e}(\psi_{TR} - F_{0,e} - \mathcal{R}_{TR}), \tag{A3}$$

where

$$\psi_{TR} = \frac{1}{1 + \xi}(F_{0,e} + \mathcal{R}_{TR} - \xi F_{0,i}), \tag{A4}$$

$$\psi_C = \bar{v}p_e^{(a)} - (p_e v)_0. \tag{A5}$$

Additionally, Equation A1, Equation A2, and Equation A3 are closed by the equations of state $p_e = k_B n T_e$ and $p_i = k_B n T_i$.

The volumetric heating rates, $E_{H,e}$ and $E_{H,i}$, are the primary degrees of freedom in our model. In the case of electron (ion) heating, $E_{H,i}(E_{H,e}) = 0$. $\bar{p}_e, \bar{p}_i$ and $\bar{T}_e, \bar{T}_i$ are the spatially-averaged coronal electron and ion pressures and temperatures, respectively and $\bar{n}$ is the spatially-averaged coronal number density. $\mathcal{R}_C = \bar{n}^2 \Lambda(T)$ is the volumetric coronal radiative loss rate, where $\Lambda(\bar{T})$ is the radiative loss function, and $\mathcal{R}_{TR} = c_1 \mathcal{R}_C$ is the radiative loss rate in the transition region where the calculation of c_1 is described in Cargill et al. (2012a). Additionally, $F_{0,e}, F_{0,i}$ are the electron and ion conductive fluxes as computed at the base of the loop, respectively, and are calculated using the classical Spitzer formula with a flux limiter imposed to prevent runaway cooling at low densities. The Coulomb collision frequency, ν_{ei}, is given by,

$$\nu_{ei} = \frac{16\sqrt{\pi}}{3}\frac{e^4}{m_e m_i}\left(\frac{2k_B \bar{T}_e}{m_e}\right)^{-3/2}\bar{n}\ln\Lambda, \tag{A6}$$

where m_e, m_i are the electron and ion masses respectively and $\ln\Lambda$ is the Coulomb logarithm. Finally, $c_2 = \bar{T}/T_a = 0.6$, $c_3 = T_0/T_a = 0.9$, determined by static equilibrium, and $\xi = \bar{T}_e/\bar{T}_i$.

Note that in the limit that $\bar{T}_e = \bar{T}_i$ such that $\xi = 1$, Equation A3 reduces to the single-fluid density equation of Cargill et al. (2012a). Additionally, Equation A1 and Equation A2 can be added together to recover the single-fluid pressure equation. As with the original EBTEL model, the modified two-fluid version has been successfully benchmarked against the HYDRAD hydrodynamic code.

REFERENCES

Bradshaw, S. J., & Cargill, P. J. 2006, Astronomy and Astrophysics, 458, 987
—. 2013, The Astrophysical Journal, 770, 12
Bradshaw, S. J., & Klimchuk, J. A. 2011, The Astrophysical Journal Supplement Series, 194, 26
Bradshaw, S. J., Klimchuk, J. A., & Reep, J. W. 2012, The Astrophysical Journal, 758, 53
Brosius, J. W., Daw, A. N., & Rabin, D. M. 2014, The Astrophysical Journal, 790, 112
Cargill, P. J. 1994, The Astrophysical Journal, 422, 381
—. 2014, The Astrophysical Journal, 784, 49
Cargill, P. J., Bradshaw, S. J., & Barnes, W. T. 2016, in preparation
Cargill, P. J., Bradshaw, S. J., & Klimchuk, J. A. 2012a, The Astrophysical Journal, 752, 161
—. 2012b, The Astrophysical Journal, 758, 5
Cargill, P. J., & Klimchuk, J. A. 2004, The Astrophysical Journal, 605, 911
Cargill, P. J., Warren, H. P., & Bradshaw, S. J. 2015, Phil. Trans. R. Soc. A, 373, 20140260
Cirtain, J. W., Golub, L., Winebarger, A. R., et al. 2013, Nature, 493, 501
Culhane, J. L., Harra, L. K., James, A. M., et al. 2007, Solar Physics, 243, 19
De Pontieu, B., Title, A. M., Lemen, J. R., et al. 2014, Solar Physics, 289, 2733
Drake, J. F., & Swisdak, M. 2014, Physics of Plasmas (1994-present), 21, 072903
Freedman, D., & Diaconis, P. 1981, Zeitschrift für Wahrscheinlichkeitstheorie und Verwandte Gebiete, 57, 453

Golub, L., Deluca, E., Austin, G., et al. 2007, Solar Physics, 243, 63
Hunter, J. D. 2007, Computing in Science & Engineering, 9, 90
Klimchuk, J. A. 2006, Solar Physics, 234, 41
Klimchuk, J. A., Patsourakos, S., & Cargill, P. J. 2008, The Astrophysical Journal, 682, 1351
Kobayashi, K., Cirtain, J., Golub, L., et al. 2011, in Society of Photo-Optical Instrumentation Engineers (SPIE) Conference Series, Vol. 8147, 81471M
Kosugi, T., Matsuzaki, K., Sakao, T., et al. 2007, Solar Physics, 243, 3
Markovskii, S. A., & Hollweg, J. V. 2004, The Astrophysical Journal, 609, 1112
Ono, Y., Yamada, M., Akao, T., Tajima, T., & Matsumoto, R. 1996, Physical Review Letters, 76, 3328
Parker, E. N. 1988, The Astrophysical Journal, 330, 474
Pérez, F., & Granger, B. E. 2007, Computing in Science & Engineering, 9, 21
Reale, F., & Orlando, S. 2008, The Astrophysical Journal, 684, 715
Reale, F., Testa, P., Klimchuk, J. A., & Parenti, S. 2009, The Astrophysical Journal, 698, 756
Reep, J. W., Bradshaw, S. J., & Klimchuk, J. A. 2013, The Astrophysical Journal, 764, 193
Schmelz, J. T., Saar, S. H., DeLuca, E. E., et al. 2009, The Astrophysical Journal Letters, 693, L131
Testa, P., De Pontieu, B., Martínez-Sykora, J., et al. 2013, The Astrophysical Journal Letters, 770, L1
Testa, P., De Pontieu, B., Allred, J., et al. 2014, Science, 346, 1255724

van der Walt, S., Colbert, S. C., & Varoquaux, G. 2011, Computing in Science & Engineering, 13, 22

Warren, H. P., Brooks, D. H., & Winebarger, A. R. 2011, The Astrophysical Journal, 734, 90

Warren, H. P., Winebarger, A. R., & Brooks, D. H. 2012, The Astrophysical Journal, 759, 141

Winebarger, A. R. 2014, AGU Fall Meeting Abstracts, 52, 03

Winebarger, A. R., Warren, H. P., Schmelz, J. T., et al. 2012, The Astrophysical Journal Letters, 746, L17

Yoo, J., Yamada, M., Ji, H., Jara-Almonte, J., & Myers, C. E. 2014, Physics of Plasmas (1994-present), 21, 055706